MECHANICAL AND ELECTRICAL PROPERTIES
OF CARBON-NANOTUBE-TEMPLATED
METALLIC MICROSTRUCTURES

by

Richard Scott Hansen

Submitted to Brigham Young University in partial fulfillment

of graduation requirements for University Honors

Department of Physics and Astronomy

Brigham Young University

June 2012

Advisor: David A. Allred

Signature: ____________________________

Honors Representative: Scott C. Steffensen

Signature: ____________________________

ABSTRACT

MECHANICAL AND ELECTRICAL PROPERTIES OF CARBON-NANOTUBE-TEMPLATED METALLIC MICROSTRUCTURES

Richard Scott Hansen

Department of Physics and Astronomy

Bachelor of Science

Microelectromechanical systems (MEMS) fabrication traditionally uses the same limited methods and materials as those used in the silicon-based microelectronics industry. In order to make MEMS out of a much richer suite of materials, such as metals, Brigham Young University researchers developed a process termed carbon-nanotube-templated microfabrication (CNT-M). In CNT-M, we grow a patterned carbon nanotube (CNT) forest and fill in the spaces between CNTs by atomistic deposition, thus creating a CNT-composite material while preserving the original pattern of the CNT forest. Through chemical vapor deposition, we have made *metallic* microstructures by infiltrating CNT forests with a tungsten or a molybdenum carbonyl precursor. We were able to infiltrate the CNT forests more completely by using the molybdenum carbonyl precursor, and we determined the electrical and mechanical properties of the resulting composite material.

Using cloverleaf test structures and the van der Pauw method, we found that the composite material has a resistivity between 749 and 935 μΩ·cm. By mechanically deflecting cantilever beams with an Instron materials testing apparatus, we found that the CNT composite has a Young's modulus between 9.17 and 56.2 GPa, a yield strength between 106 and 221 MPa, and a maximum percent strain between 0.4 and 1.5%. These results characterize the material as being both electrically conductive and mechanically strong. Therefore, this simple, yet effective, method for creating metallic microstructures could open the door to new possibilities for MEMS.

ACKNOWLEDGMENTS

None of this work would have been possible if it weren’t for the help and tutelage given to me by the students in my research group, such as David McKenna, Jason Lund, Taylor Wood, Kyle Zufelt, Adam Konneker, Walter Fazio, and Kyle Anderson, and I wish to thank each of them for all that they have done for me. I owe a debt of gratitude to the faculty in my research group, Drs. Robert Davis, Richard Vanfleet, and David Allred, who have played key roles in helping me direct my research and writing efforts while at the same time giving me good examples to follow in my personal life. In addition, I need to thank Shauna Barrick from Brigham Young University’s Honors Department for continually going the extra mile in her efforts to help me graduate with University Honors. I am especially grateful for all the generous research funding I received from Brigham Young University’s Department of Physics & Astronomy, as it made it much easier for me to afford to do the things that I love. Finally, I wish to thank my family for the inspiration and support they have been for me, because I couldn’t have done this without them.

TABLE OF CONTENTS

LIST OF FIGURES

LIST OF TABLES

Chapter 1

Introduction

1.1 Carbon Nanotubes

Among the many discoveries published in modern science and technology, few have revolutionized their field as much as the exposition on carbon nanotubes (CNTs) by Sumio Iijima in 1991 [1]. In essence, CNTs are sheets of graphene that have been seamlessly rolled into long, hollow cylinders. Single-walled CNTs (SWNTs) consist of a single-layered tube of graphene, whereas multiwalled CNTs (MWNTs), herein referred to as CNTs for simplicity, consist of two or more concentric SWNTs (see Figure 1.1). Due to the unique structure of CNTs, theoretical calculations, which have been confirmed experimentally, show that CNTs

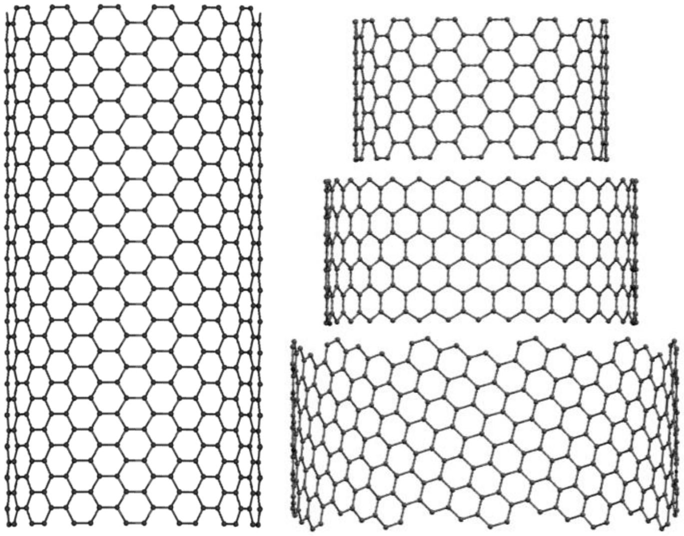

Figure 1.1 Computer-generated models of CNTs. On the left is an “armchair” SWNT, and on the right is a MWNT composed of the three possible SWNT structures, “armchair,” zigzag,” and “chiral.” The concentric tubes are separated so as to clearly distinguish the structure of each layer. Their names come from the shape of the tubes’ top edges. Images are thanks to Brigham Young University student Conrad Rosenbrock.

have incredible mechanical, electrical, and thermal properties [2-3]. Their quasi-one-dimensional nature, with diameters on the order of nanometers and lengths up to one centimeter, coupled with their unprecedented Young's modulus, large tensile strength, and high electrical and thermal conductivities, make them one of the most desirable materials in nanoscale engineering and electronics.

In order to fully exploit CNTs' exceptional characteristics, the worldwide scientific community is continually trying to find more precise ways to control the production of CNTs and has developed many growth methods, such as by arc discharge, laser ablation, and chemical vapor deposition [4]. In addition, researchers regularly strive to innovate new ways to implement CNTs in the world of science and technology. Individual CNTs have been used as field-effect transistors (FETs), atomic force microscopy (AFM) tips, nanoneedles for drug delivery and cancer treatment, and electronic nanowires and switches, whereas arrays of CNTs have been utilized as field emitters, supercapacitors, lithium ion battery anodes, optically transparent electrodes, fuel cells, and filters [5-9]. In fine, CNTs are becoming an integral part of the continually evolving world of science and technology.

1.2 Microelectromechanical Systems

In fulfillment of the predictions made by men like Richard Feynman and Gordon Moore, modern technology is continually becoming faster, stronger, lighter, and more compact [10-12]. On the cutting edge of technology and engineering is the realm of microelectromechanical systems (MEMS). At times referred to as microdevices, MEMS are tiny electromechanical devices with dimensions on the order of micrometers. From transportation, communication, and defense to gaming, entertainment, and medicine, MEMS have applications everywhere. They are becoming more and more commonplace in today's technologies and are used as accelerometers in airbags, gyroscopes in cell phones, pressure and flow sensors in medical equipment, thermal detectors in computers, and inkjet printer heads in modern printers [13].

Like the majority of today's most advanced technologies, MEMS development has faced many difficult challenges. In contrast with conventional electromechanical systems, where optimizing fabrication, performance and cost determines which methods and materials would be best, MEMS fabrication traditionally uses the same methods and materials as those used in the silicon-based microelectronics industry. Having a high aspect-ratio (height-to-width) is one particularly desirable trait for MEMS, because it allows for more surface area between interacting components and prevents out of plane motion. The two most successful high-aspect-ratio microfabrication techniques are deep reactive ion etching (DRIE) and LIGA (a process combining X-ray lithography, electroplating, and micromolding) [14-15]. However, these techniques are both fairly cost-prohibitive and limited in their fabrication materials selection. Therefore, a high-aspect-ratio microfabrication process that is both cost-effective and compatible with a wide variety of materials, such as metals, would open the door to a world of possibilities for MEMS.

One avenue of help for fabricating electromechanical devices on the microscale is in utilizing advanced nanomaterials. For example, as discussed in the previous section, CNTs can easily serve as nanowires and probes in many advanced technological applications where traditional fabrication methods are becoming insufficient. In addition, researchers have found that, in place of silicon, arrays of CNTs can be used as a material for fabricating MEMS [16-17]. In this thesis, I will report on using vertically-aligned CNTs as scaffolding for creating metallic microstructures.

1.3 Carbon-Nanotube-Templated Microfabrication

In order to make high-aspect-ratio MEMS out of a much richer suite of materials, including metals, semiconductors and ceramics, Brigham Young University researchers developed a process termed carbon-nanotube-templated microfabrication (CNT-M) [18]. This method employs patterned, vertically-aligned CNT forests as a three-dimensional microfabrication scaffold to create precise, high-aspect-ratio microstructures. The "as grown," low-density CNT structures are not useful as mechanical materials because they are extremely fragile, consisting mostly of air. However, by filling the voids between CNTs with a secondary material through atomistic deposition, the infiltrated CNT framework becomes a robust, high-aspect-ratio microstructure consisting mostly of the filler material. Thus, CNT-M is a hybridized version of microfabrication, creating microscale structures by combining CNTs, an advanced nanomaterial, with thin-film technology. The advantage of CNT-M is that existing thin-film technologies can be applied to create solid structures with dimensions much larger than those possible by thin-film deposition alone.

Using the CNT-M method, semiconductors (Si and a-C) and dielectrics (SiO_2 and Si_3N_4) are shown to successfully deposit within the CNT framework [19-20]. In addition, functional MEMS, such as cantilever beams, bistable mechanisms (BSMs), thermomechanical in-plane microactuators (TIMs), and cell-restraint devices, have been fabricated by CNT-M and tested (see Figure 1.2) [21-22]. However, the electrical properties of the composite materials made by CNT-M in these previous studies are either unsuitable for low-resistance applications or unreported. Therefore, a study of CNT-M using metals was necessary.

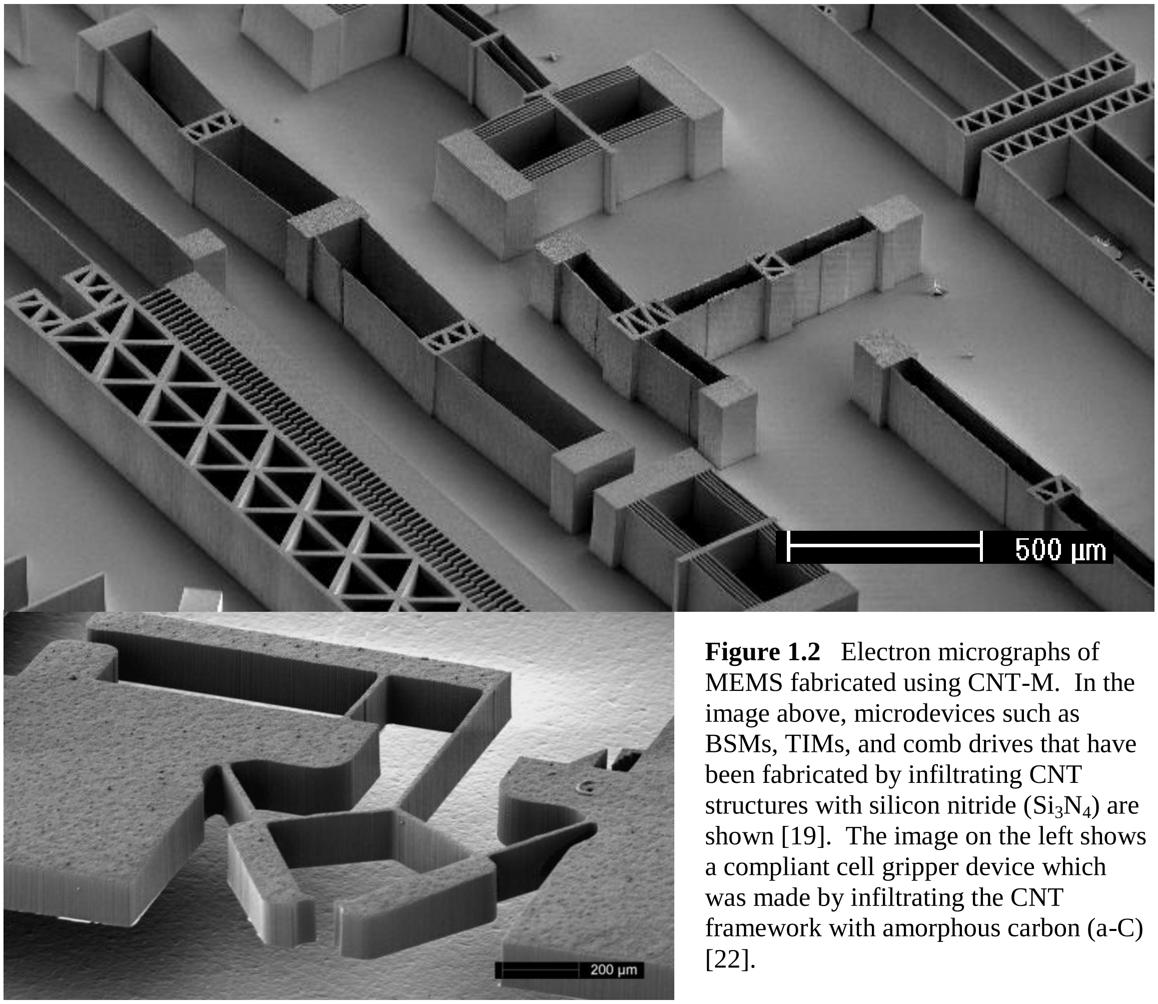

Figure 1.2 Electron micrographs of MEMS fabricated using CNT-M. In the image above, microdevices such as BSMs, TIMs, and comb drives that have been fabricated by infiltrating CNT structures with silicon nitride (Si_3N_4) are shown [19]. The image on the left shows a compliant cell gripper device which was made by infiltrating the CNT framework with amorphous carbon (a-C) [22].

1.4 Chemical Vapor Deposition of Metal Carbonyls

In order to expand the materials selection for CNT-M to metals, David McKenna, a Brigham Young University student, adapted a previously constructed chemical vapor deposition (CVD) chamber and tested it using a tungsten carbonyl precursor ($W(CO)_6$) [23-24]. His work laid the foundation for the research represented by this thesis and led us to further explore depositing metals within the CNT framework by using molybdenum carbonyl ($Mo(CO)_6$) as the CVD precursor, and to experimentally determine the mechanical and electrical properties of the resulting CNT composite material.

Metal carbonyls such as $Mo(CO)_6$ have been used to create metallic thin films for over 65 years [25]. Hexacarbonyls, like $Mo(CO)_6$, have a central metal atom surrounded by six carbon monoxide (CO) molecules (see Figure 1.3). They generally come in a

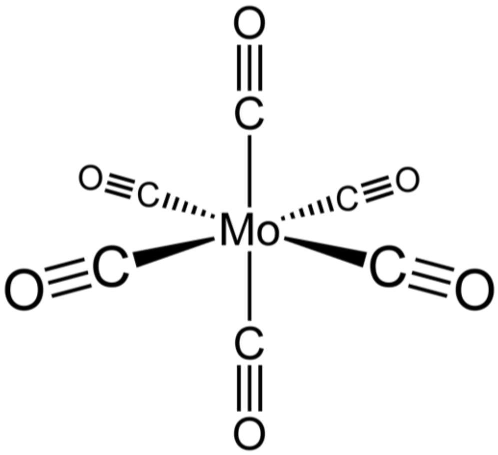

Figure 1.3 Molybdenum Carbonyl ($Mo(CO)_6$). Above we see a perspective drawing of a $Mo(CO)_6$ molecule showing its octahedral structure, with a molybdenum atom in the center and six carbon monoxide molecules at its octahedral sites (image taken from Wikipedia). To the right is a photograph taken of a bottle of $Mo(CO)_6$, and in the petri dish we see $Mo(CO)_6$ in its powder form.

powder form, and when they are used as a CVD precursor the process is referred to as metal-organic or organometallic. Since refractory metals such as molybdenum have melting points higher than almost any other material, the development of a metal-organic CVD technique for these materials, which is effective at temperatures far below the metals' melting points, has been very useful in many technological applications [26].

In order to deposit thin films via metal-organic CVD, carbonyl powder must first volatilize into a gas phase, then pyrolyze, causing some of the CO molecules to disassociate from the rest of the carbonyl molecule, and finally adsorb onto the desired substrate [27]. The resulting films inherently contain carbon and oxygen impurities, and their deposition-temperature-dependent compositions include metal oxides, carbides, and oxycarbides, while some authors even report obtaining pure metals [28-29]. In the case of molybdenum carbonyl, it is important to note that under deposition conditions similar to those used for the research in this thesis, the resulting metal film is reported to have a molybdenum oxycarbide (MoO_xC_y) structure and an electrical resistivity of 250 ± 25 $\mu\Omega\cdot$cm [30].

Chapter 2

Experimental Methods

2.1 CNT-M Overview

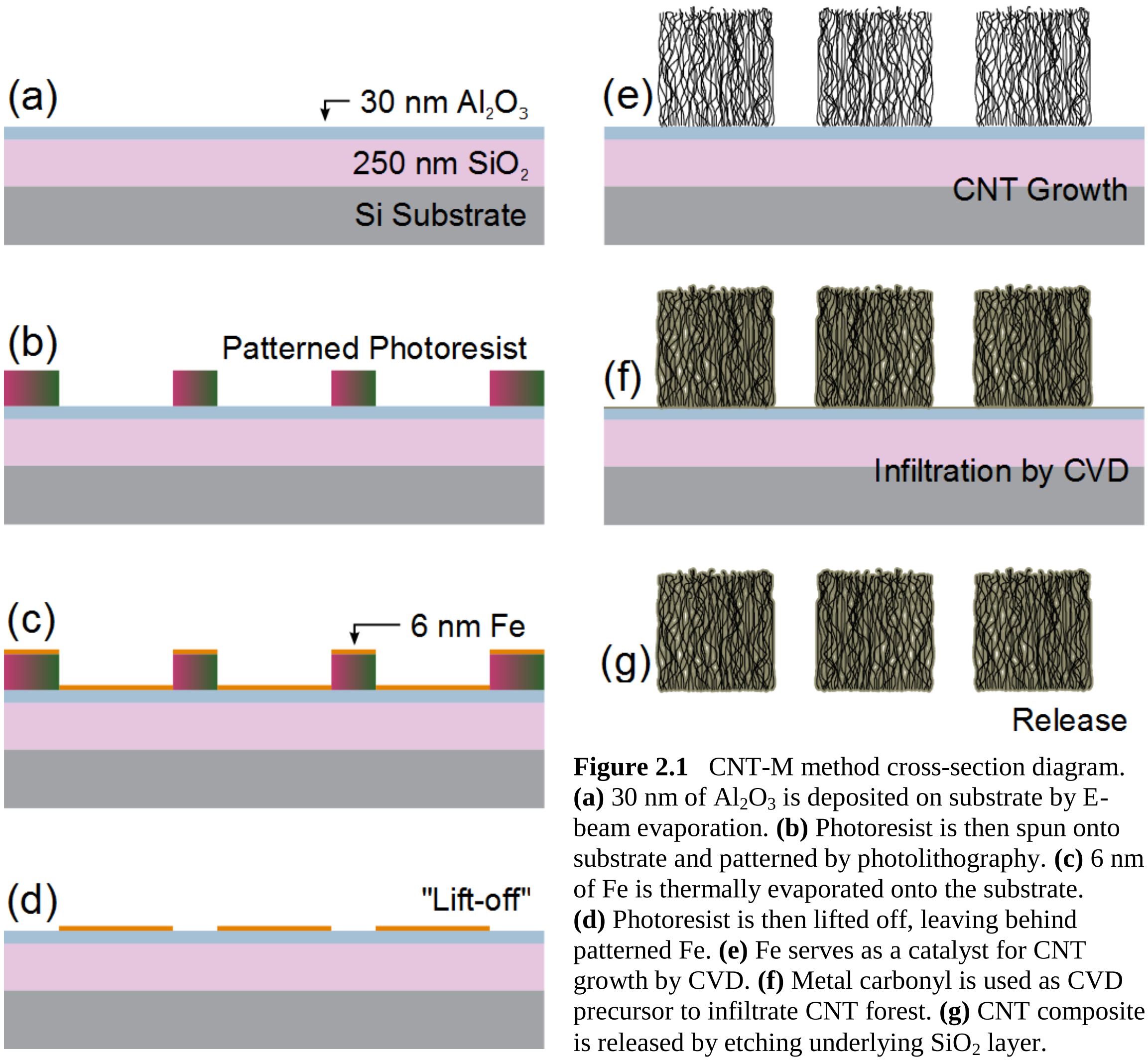

Figure 2.1 CNT-M method cross-section diagram. **(a)** 30 nm of Al_2O_3 is deposited on substrate by E-beam evaporation. **(b)** Photoresist is then spun onto substrate and patterned by photolithography. **(c)** 6 nm of Fe is thermally evaporated onto the substrate. **(d)** Photoresist is then lifted off, leaving behind patterned Fe. **(e)** Fe serves as a catalyst for CNT growth by CVD. **(f)** Metal carbonyl is used as CVD precursor to infiltrate CNT forest. **(g)** CNT composite is released by etching underlying SiO_2 layer.

2.2 CNT Growth

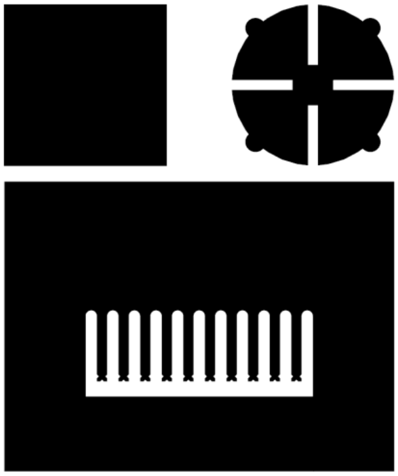

Figure 2.2. Top-down view of the photolithography mask used to define the shape of the test structures made for determining the materials properties of the metal-CNT composite material. The structure on the top right is a van der Pauw clover leaf for testing the electrical resistivity. The one on the bottom is a cantilever structure for force testing. The square on the top left is 0.5 by 0.5 cm in size.

Following the standard procedure used at Brigham Young University for the patterning and growth of vertically-aligned CNTs, we first deposited a 30 nm layer of alumina (Al_2O_3) onto a silicon wafer through E-beam evaporation. Next, we spun a 1 μm thick layer of AZ 3312 photoresist, a photosensitive material, onto the substrate. We then subjected the exposed photoresist to high-intensity ultraviolet light with a patterned mask (see Figure 2.2) and developed the photoresist in AZ 300 MIF developer. Developing the photoresist left the unexposed layer of photoresist on the substrate and revealed the underlying layer of alumina in the mask's pattern. Next, we deposited 6 nm of iron on the substrate through thermal evaporation, and we verified the thickness indicated by the thermal evaporator's crystal monitor using atomic force microscopy. Finally, we performed liftoff with Microposit 1165, which removed the remaining photoresist, thus leaving iron in the desired pattern for the catalyst bi-layer of alumina and iron for CNT growth.

The actual CNT growth required that we heat the sample from room temperature to 750°C in about 10 minutes while flowing 500 sccm of hydrogen (H_2), and then, while maintaining the sample temperature at 750°C, add 700 sccm of ethylene (C_2H_4) until the nanotubes had grown to the desired height. For the test structures used for strength and electrical measurements, we grew the nanotubes with C_2H_4 flowing for 10 seconds, which resulted in a growth height of about 15 μm.

2.3 Infiltration

The CNT framework was infiltrated in a CVD chamber that had been pumped down to a pressure of about 1.75 Torr (see Figure 2.3). We heated the sample holder while monitoring its temperature with a thermocouple. Once the sample reached the desired temperature, we then began flowing 50 sccm of H_2 gas and, with a cartridge heater, heating the block containing the $W(CO)_6$ or $Mo(CO)_6$ precursor to 160°C.

By watching the chamber pressure gauge, we could determine when the carbonyl precursor began to volatilize. This was indicated by an increase in pressure. When the carbonyl precursor was gone, either from being deposited on the substrate or evacuated

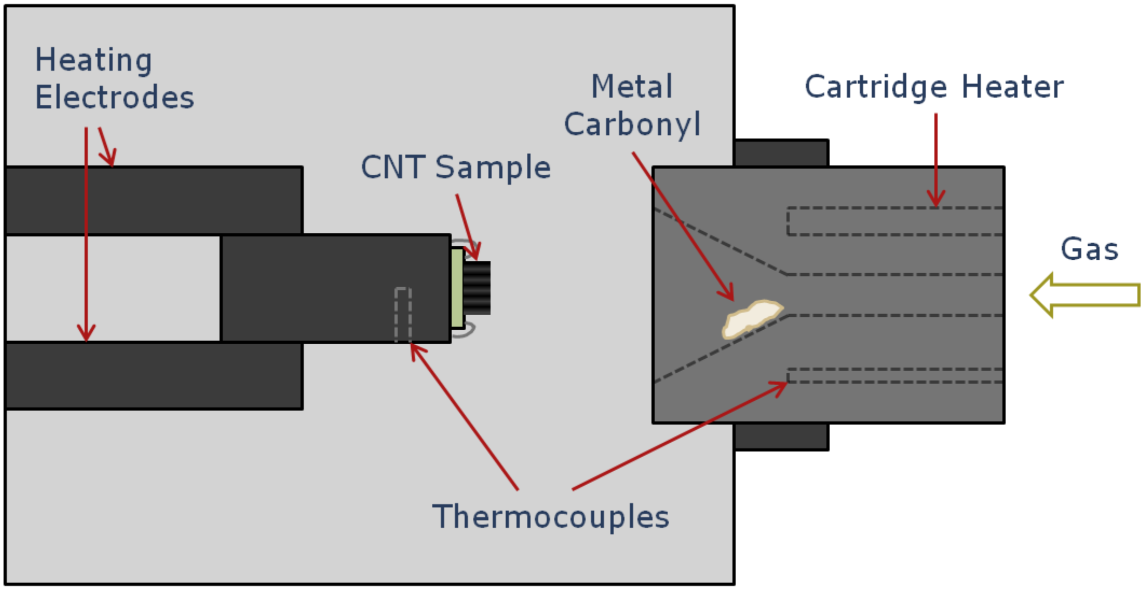

Figure 2.3 Schematic of our CVD deposition chamber. We secure the CNT sample to a heating block and monitor its temperature with a thermocouple embedded in the aluminum sample holder. The metal carbonyl is placed on a heating block, through which flows H_2 gas.

out of the chamber, the pressure returned to normal. Once the carbonyl had been depleted, as noted by the pressure returning to pre-deposition levels, we turned off the heaters and allowed the sample to cool in 25 sccm of flowing H_2 gas.

In order to optimize the infiltration of the CNT framework, we tried sample temperatures ranging from 200 to 350°C while varying the amount of carbonyl placed in the CVD chamber between 2 to 6 grams for $W(CO)_6$ and 1 to 2 grams for $Mo(CO)_6$. In each case we roughly determined the strength, and thus extent of infiltration, of the resulting CNT composite using a scratch test. Since an uninfiltrated CNT forest easily brushes away with the slightest touch of tweezers, we could tell whether there was a fair amount of infiltration by scratching the CNT forest with tweezers and seeing if it stayed together. Those samples that we desired to further investigate were then examined by scanning electron microscopy. Specifically, we looked at the extent of infiltration and measured the dimensions of the test structures for later use in determining the material's electrical and mechanical properties.

2.4 Release

The silicon wafers used in CNT growth had about 250 nm of thermally-grown SiO_2 on top which could serve as a release layer. In order to release the composite structures from the silicon wafer for mechanical testing, we etched away the SiO_2 by placing the samples in 48% diluted hydrofluoric acid for about 20 minutes, or until the test structures had clearly released from the substrate.

2.5 Electrical Testing

In order to determine the composite material's electrical resistivity, we performed a systematic four-point probe test on cloverleaf structures using the van der Pauw method [31], making eight different measurements per van der Pauw cloverleaf structure (see Figure 2.4). A number of distinct measurement geometries are possible with four contacts, so we used a reference system to keep track of our measurements. We numbered the cloverleaf contact points 1-4 counterclockwise starting in the top left corner. Then we labeled each current measurement by where we injected the current and where we took it out (i.e., current I_{12}, from contact 1 to contact 2). Similarly, we labeled our voltage measurements according to the contacts used in measuring that voltage (i.e., voltage V_{34}, between contact points 3 and 4). In making a measurement, we would flow

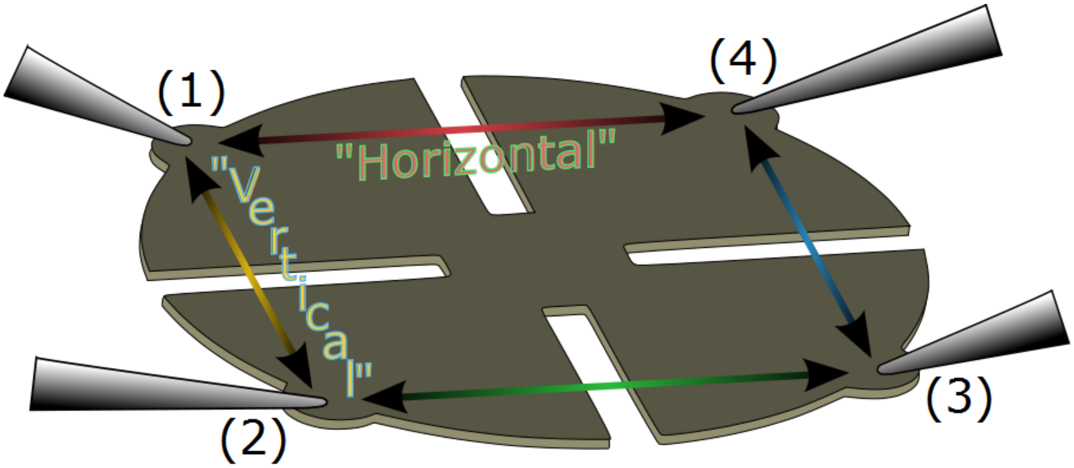

Figure 2.4 Electrical testing setup. We labeled the four contact points 1-4 in the counterclockwise direction and used them for distinguishing between our various measurements. For example, a measurement in the vertical direction consisted of flowing a current into point 1 and taking it out of point 2 ($\boldsymbol{I_{12}}$) while measuring the voltage across points 3 and 4 ($\boldsymbol{V_{34}}$). A reversed polarity measurement required that we reverse the direction of the current ($\boldsymbol{I_{21}}$) and obtain a voltage measurement ($\boldsymbol{V_{43}}$). Reciprocal measurements could be obtained in both cases by swapping the current and voltage contacts ($\boldsymbol{I_{34}}$ and $\boldsymbol{V_{12}}$, and $\boldsymbol{I_{43}}$ and $\boldsymbol{V_{21}}$). We made measurements in both the vertical and horizontal directions and then averaged their values to account for any errors and obtain a more reliable measurement.

a current through half of the sample and measure the voltage drop across the other half, and then using Ohm's law we could calculate a resistance (i.e., $R_{12,34} = \frac{V_{34}}{I_{12}}$).

Using micromanipulators, we carefully positioned four tungsten probe tips in contact with the cloverleaf structure's outside-edge reference dots, one on each leaf (see Figure 2.4). Then we performed both reciprocal and reversed polarity resistance measurements in the "vertical" and "horizontal" directions (four measurements per direction), and after obtaining average values for $R_{vertical}$ and $R_{horizontal}$, we determined the sheet resistance, R_{sheet}, by the van der Pauw formula [31]:

$$e^{-\pi R_{vertical}/R_{sheet}} + e^{-\pi R_{horizontal}/R_{sheet}} = 1. \tag{2.1}$$

When the sample and setup are adequately symmetrical, $R_{vertical} = R_{horizontal} = R$, and thus the van der Pauw formula simplifies to give

$$R_{sheet} = \frac{\pi R}{\ln 2}. \tag{2.2}$$

Finally, knowing R_{sheet} and the sample's thickness, t, we obtained values for the resistivity:

$$\rho = R_{sheet} t. \tag{2.3}$$

2.6 Mechanical Testing

We determined the mechanical properties of the infiltrated CNT composite using cantilever beams and an Instron 3342 materials testing apparatus. The Instron apparatus functions by lowering a needle onto the cantilever while measuring the force on the needle per millimeter of deflection. After placing a cantilever beam in the Instron apparatus, we aligned the needle so that it came in contact with the end of the beam in the center of the alignment markings (see Figure 2.5). The Instron slowly depressed each cantilever beam at a rate of 0.5 mm/minute until the beam broke.

Using the data recorded by the Instron apparatus, we calculated values for the Young's modulus, yield strength, and maximum strain of the material by applying linear beam theory for a singly-clamped beam:

$$E = \frac{4Fl^3}{dwt^3}, \tag{2.4}$$

$$\sigma = \frac{6F_{max}l}{wt^2}, \tag{2.5}$$

and

$$\varepsilon = \frac{\sigma}{E} = \frac{3dt}{2l^2}, \tag{2.6}$$

respectively, where F is the applied force, d the elastic deflection, F_{max} the force when the beam fails, l the beam's length, w its width, and t its thickness [32].

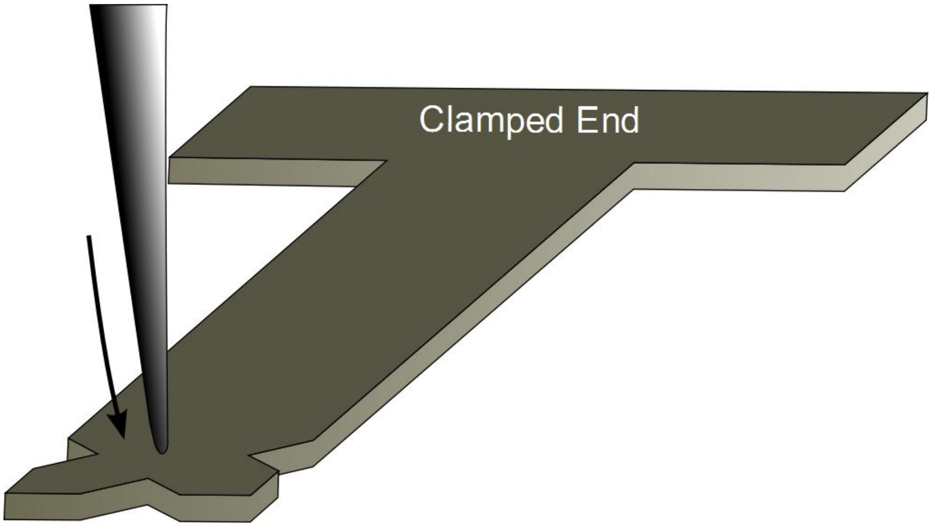

Figure 2.5 Mechanical testing setup. We clamp a cantilever beam at its base, and then, with the aid of a microscope, we center a needle over the end of the cantilever. The Instron apparatus slowly lowers the needle, thus deflecting the cantilever beam, and records the force exerted on the needle per deflection.

Chapter 3

Discussion of Results

3.1 CNT Growth and Infiltration

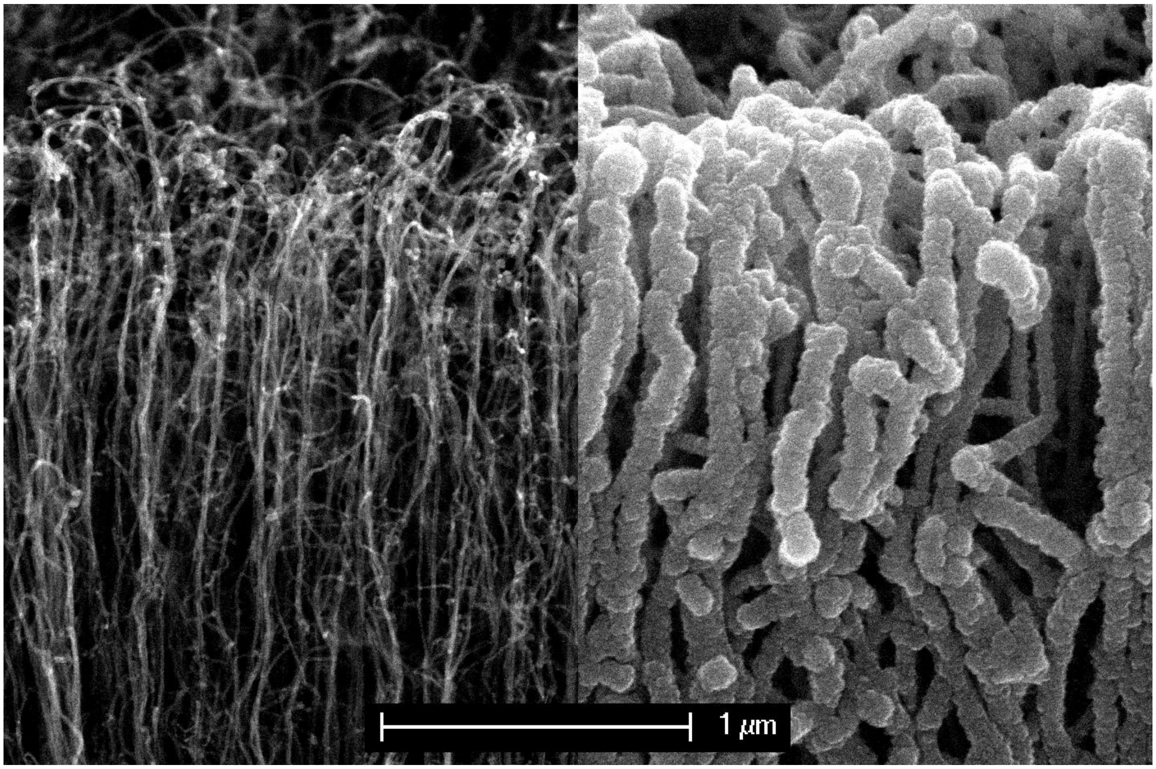

Figure 3.1 CNTs before and after infiltration. On the left are pristine CNTs prior to being coated through CVD, and on the right is the same sample after infiltration with $Mo(CO)_6$. Although each individual CNT is coated conformably, the coated CNTs begin to bundle together as the infiltration progresses, thus forming a more cohesive structure. Images were taken at a 30° tilt.

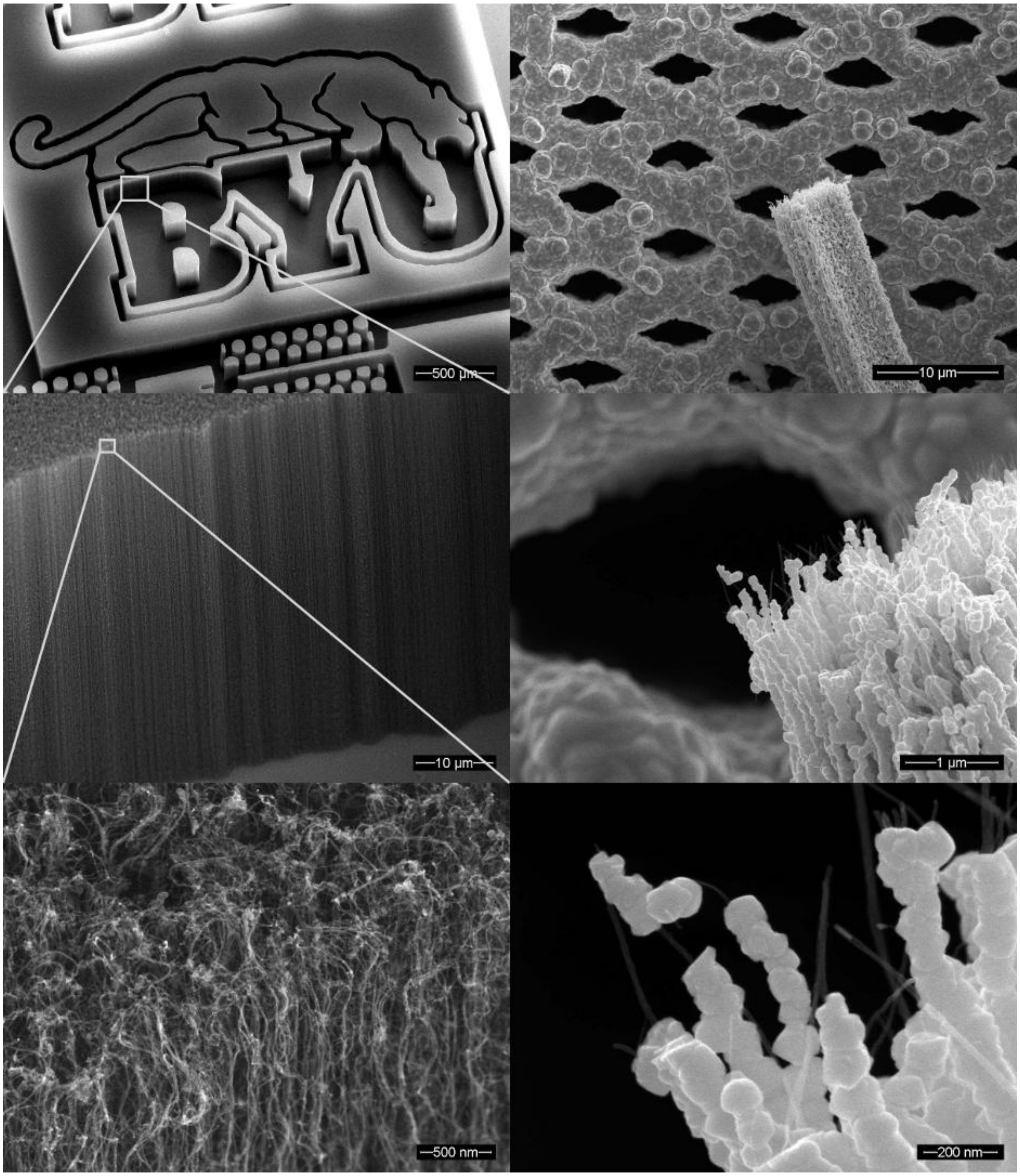

Figure 3.2 Patterned CNT forests with and without infiltration. On the left is a series of images taken at a 30° tilt showing how a patterned forest of CNTs can have a high aspect-ratio in virtually any shape, which in this case was a BYU Cougar logo. On the right is a series of top-down images showing a microfilter pattern that has been infiltrated with $W(CO)_6$. The pillar being zoomed in on is a piece of the filter that has been broken with tweezers.

3.2 Film Stress and Extent of Infiltration

During the early stages of optimizing the forest infiltration, we observed that the stresses present in the infiltrated structures were at times powerful enough to tear apart the CNT framework. In particular, we noticed that the overall stress acting on the structures was greatest when the deposited metal oxycarbide film quickly plugged up the top and sides of the CNT forest, forming a thick capping layer on the outside of the structure while leaving the inside only slightly infiltrated (see Figure 3.3).

In order to decrease the stress caused by thick capping layers, we experimented with two approaches: decrease the amount of available carbonyl precursor while holding the temperature constant, and decrease the substrate temperature while using the same

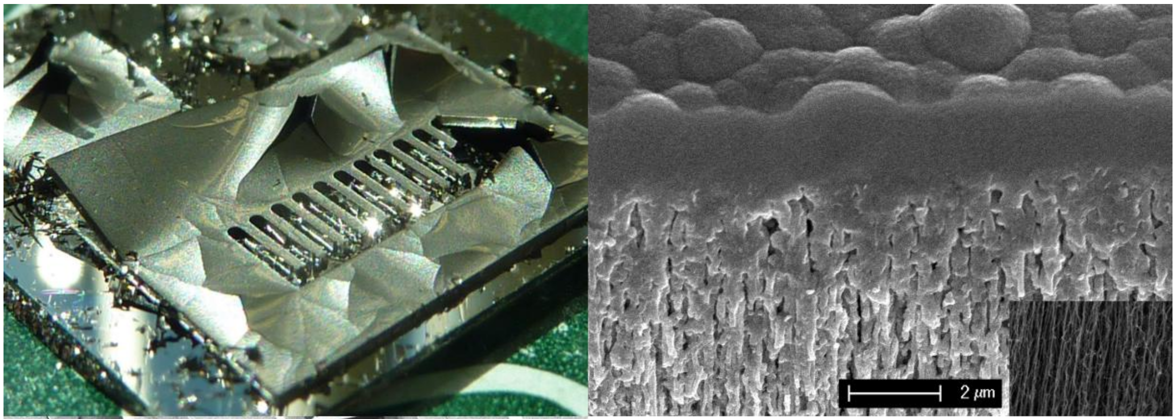

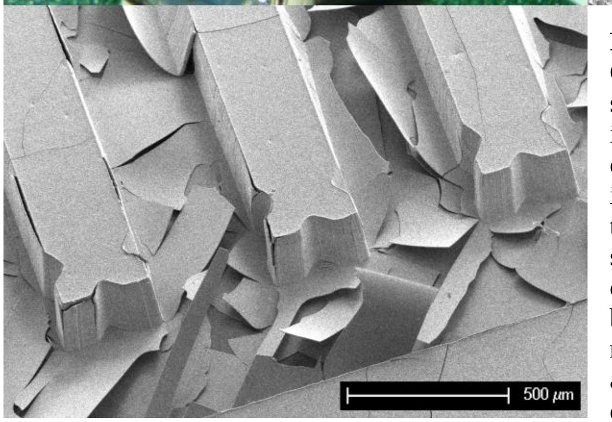

Figure 3.3 CVD capping layer and its effects on CNT structures. Each image is of the same test sample that had been infiltrated with $Mo(CO)_6$. The images on the left show how the CNT structures cracked and exploded outwards during the infiltration process. The mudflat-like cracking of the deposited MoO_xC_y layer in the bottom left scanning electron micrograph is evidence that the cantilever beams and the floor layer between the beams underwent high tensile stress. On the top right is a cross-sectional image of the CNT forest and deposited capping layer, and inset is an image of the underinfiltrated inside of the forest.

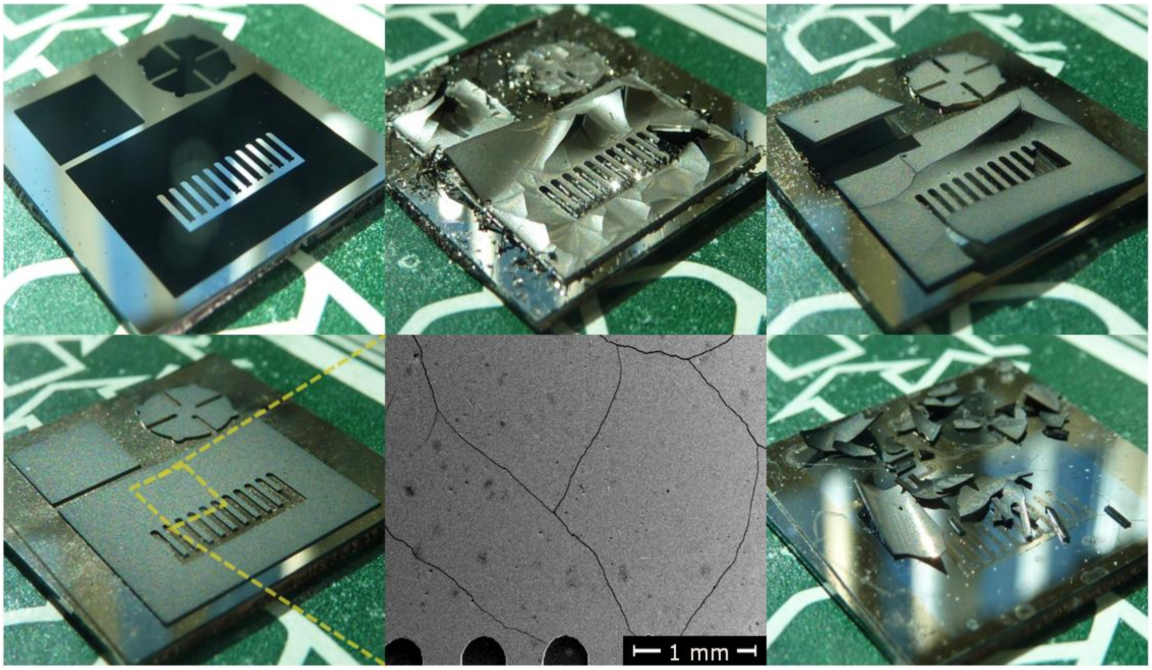

Figure 3.4 Decreasing film stress. Top-left is a photograph of CNT test structures prior to infiltration with Mo(CO)$_6$. The top-middle and top-right images show post-infiltration CNT structures that underwent enough tensile stress to tear apart and delaminate from the silicon substrate. Bottom-left we see CNT test structures that survived the infiltration process, but as the bottom-center scanning electron micrograph shows, the tensile stress still present was enough to cause microcracking. Upon releasing the structures from their substrate, the microcracks caused them to fall apart, as seen at the bottom-right.

amount of carbonyl (see Figure 3.4). Holding temperature constant while we decreased the amount of carbonyl in the system effectively shut off the deposition before a thick capping layer could occur. However, this did not fix the tendency for the majority of the deposition to occur on the outside of the CNT structures.

In order to describe this challenge, it is useful to consider the concept of the carbonyl molecule having a sticking coefficient, or the probability that at a given temperature a carbonyl molecule will pyrolyze and deposit when it comes into contact with the sample. For samples with far more deposition on the forest tops and outside edges, one could say that the sticking coefficient was high, or that the first time the carbonyl bounced into the sample was likely to cause pyrolysis and deposition. On the other hand, if the sticking coefficient was low, then the carbonyl molecule was likely to bounce a number of times and have a greater opportunity to diffuse deep into the CNT forest before finally undergoing pyrolysis and depositing onto the sample. As a result, the infiltration then becomes more even throughout the sample thickness, and so too do the stresses present in the sample. The only way we have successfully decreased the sticking coefficient is by lowering the sample's temperature, and in general, we saw that the more evenly infiltrated samples were able to withstand the stresses present inasmuch as there was no capping layer.

After much experimentation, we determined that there were optimums for $W(CO)_6$ and $Mo(CO)_6$ where the sticking coefficient was low and yet the deposition rate was fairly high, and thus the amount of carbonyl needed was low. When using $W(CO)_6$ as the CVD precursor, the optimum was using about 2 grams of carbonyl while holding the sample temperature around 290°C. In the case of $Mo(CO)_6$, sample temperatures between 214 and 220°C with about 1.45 grams of carbonyl were what provided the best infiltration. We found that the optimum for $Mo(CO)_6$ was more ideal than the optimum for $W(CO)_6$, because it required less carbonyl, used a lower temperature, and provided a more uniform infiltration throughout the forest than what we could achieve using $W(CO)_6$. For both $W(CO)_6$ and $Mo(CO)_6$, there were other deposition parameters of the "sweet spot," such as the ideal pressure and which gasses to introduce during the deposition run, that are not known.

We used a variety of patterned CNT samples during our early efforts to maximize the infiltration, and we found that we could attain a good infiltration with $W(CO)_6$ using high-aspect-ratio structures, such as microfilters, inasmuch as the maximum infiltration distance was less than 3 μm (see Figure 3.5). However, when we attempted to infiltrate the test structures, which have a lower aspect-ratio and longer diffusion distances, the

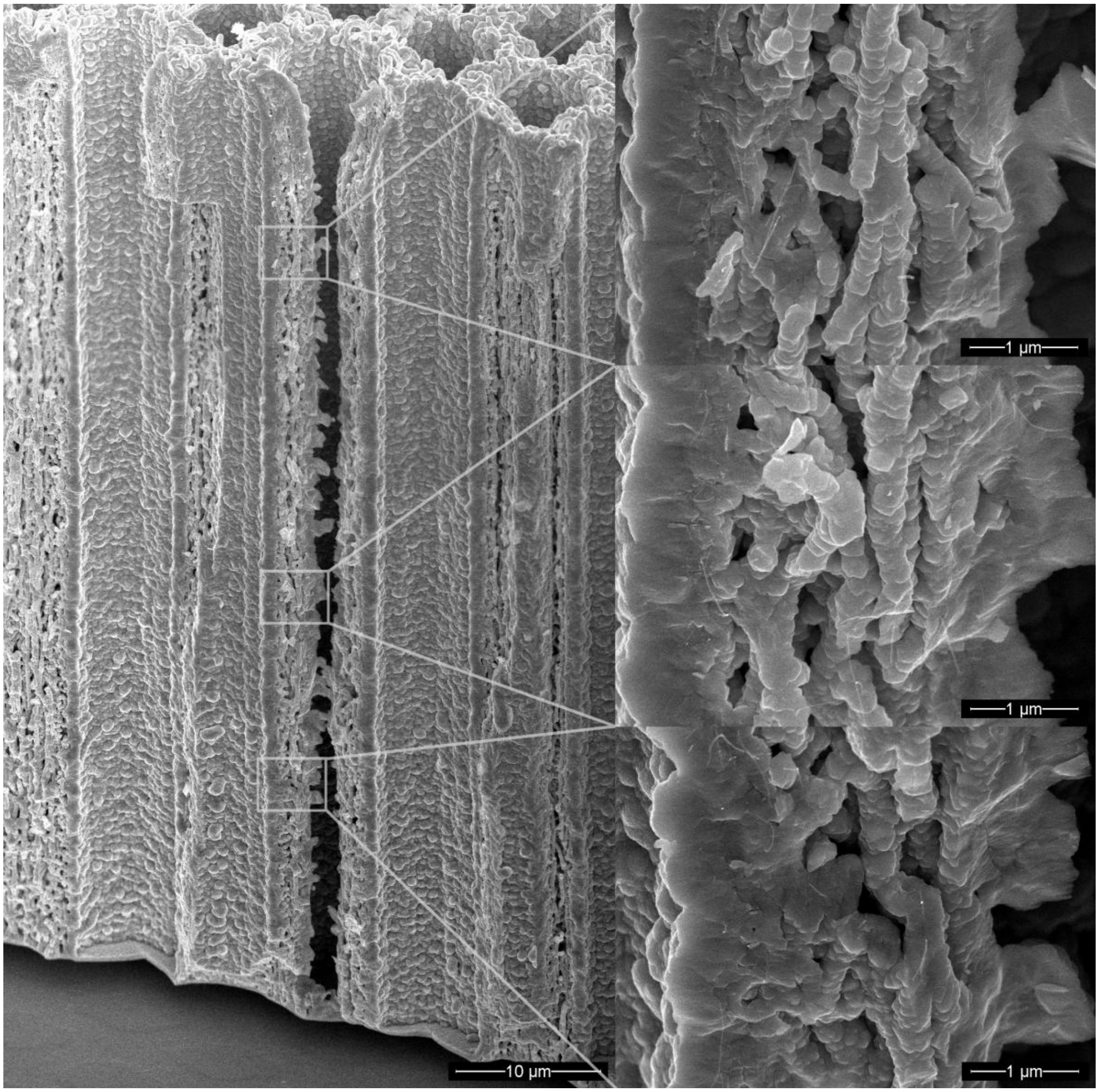

Figure 3.5 Microfilter pattern infiltrated with $W(CO)_6$. These images are of a break in the sample made to determine the extent of infiltration inside the CNT forest. The high-aspect-ratio filter pattern provides vapor access holes for the carbonyl molecules to readily diffuse to the bottom of the forest before depositing. Note how the extent of infiltration is uniform throughout the height of the forest.

optimum failed to infiltrate adequately enough for the samples to undergo any meaningful electrical or mechanical testing, due to their fragility (see Figure 3.6). On the other hand, the optimum for $Mo(CO)_6$ was efficient enough at infiltrating the CNT forests that we were eventually able to successfully release some test structures.

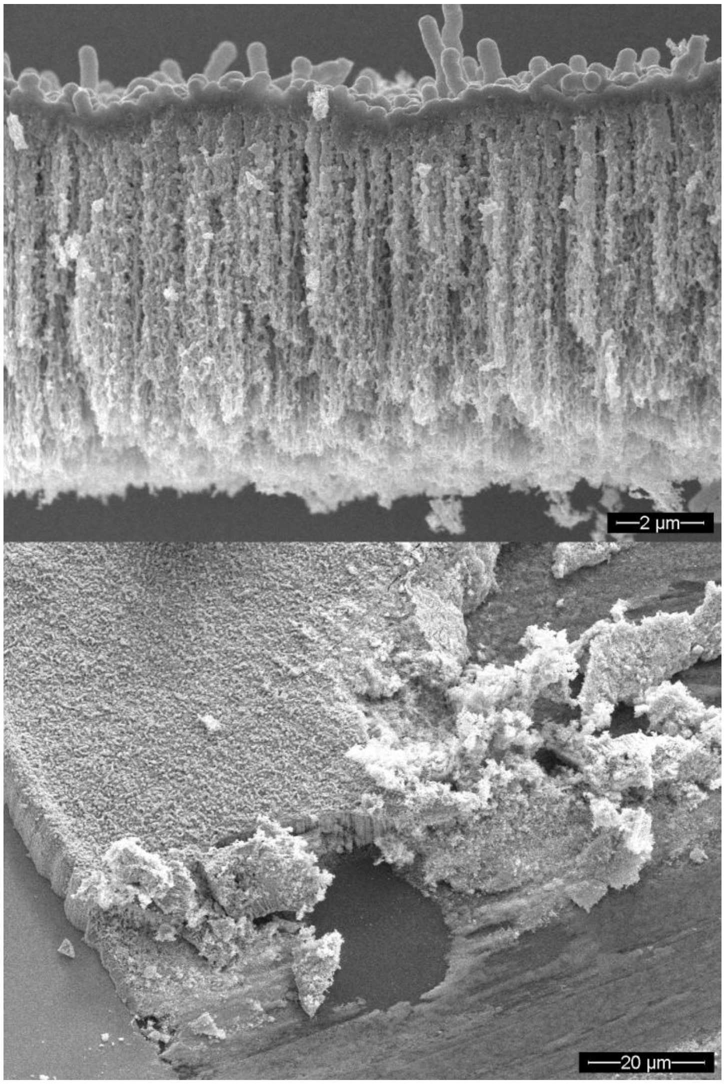

Figure 3.6 Test structures infiltrated with $W(CO)_6$. Using the best deposition parameters we could, we infiltrated a test structure sample with $W(CO)_6$. We found that the sticking coefficient for $W(CO)_6$ was too high to achieve uniform deposition for our test structures, as evidenced in the top scanning electron micrograph of the forest's cross-section by the strong deposition gradient, and in the bottom image, which shows how the CNT structure crumbled during the tweezers scratch test. Better-infiltrated forests tended to snap and chip during the scratch test rather than crumble like this sample.

Although depositions performed using the $Mo(CO)_6$ CVD precursor were the best observed, the sticking coefficient *was* high enough that for large structures with long diffusion distances there were still differences in the extent of infiltration between the outside edges of the structures and the insides. Therefore, in order to achieve as uniform an infiltration as possible, we chose to decrease the maximum diffusion distance with the hope that the deposition gradients would lessen. To this end, we used shorter forest heights (about 15 μm). The results were much better (see Figure 3.7).

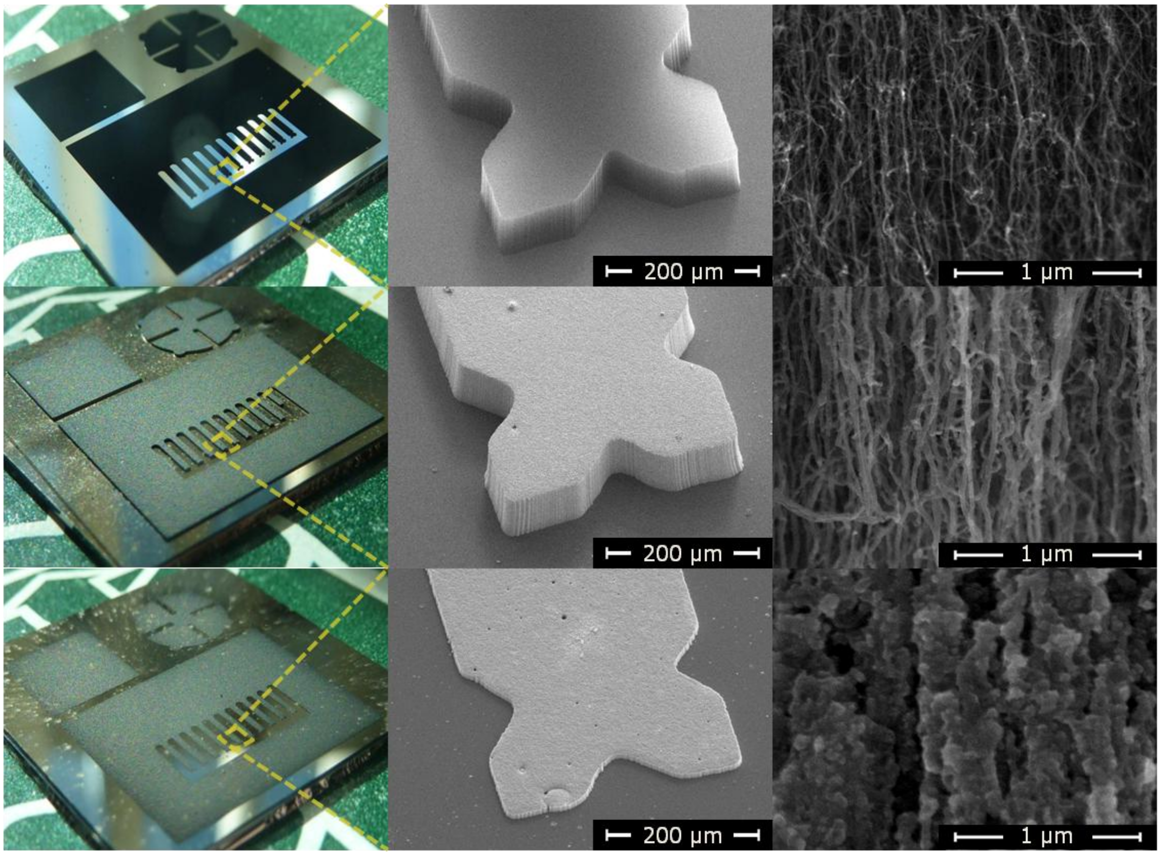

Figure 3.7 Improving the extent of infiltration by decreasing the forest height. The images on the top row are of patterned CNTs prior to infiltration. The middle row shows post-deposition images of a CNT forest that is about 100 μm tall, and in the bottom row are images of an infiltrated forest that was only about 13 μm tall. The scanning electron micrographs in the far right column are cross-sectional images from deep inside the CNT forests. Note how the infiltration from within the taller forest was almost nominal, whereas the shorter forest was almost completely filled.

3.3 Resistivity

Although we were unable to infiltrate test samples with $W(CO)_6$ well enough for electrical and mechanical testing, we did successfully test samples infiltrated with $Mo(CO)_6$. Therefore, all of our data is representative of the MoO_xC_y-CNT composite material only.

Because we expected the CNT composite to be isotropic in the plane perpendicular to the CNTs, we assumed that, for a given van der Pauw disk, the resistivity measurements should be the same for all eight of the four-point probe configurations. As expected, resistance measurements were very uniform for each sample. In addition, we found that the van der Pauw method was very effective for ensuring that each of the four probes had good electrical contact with the cloverleaf structures. When for the same van der Pauw disk we detected large differences between the various resistance measurements, we double-checked the probes' contacts, and in each case we found that there had been a poor connection.

We found that the MoO_xC_y-CNT composite material had a resistivity between 749 and 935 $\mu\Omega\cdot$cm, about 3-4 times greater than bulk MoO_xC_y. We theorize that the resistivity is greater in our case due to the voids in the CNT composite. Although CNTs usually have a very high conductivity (and thus low resistivity), their contribution to the conductance in the sample was not sufficient enough to compensate for the decrease in conductivity caused by the voids.

With its low resistivity, this MoO_xC_y-CNT composite material could be used to create metallic MEMS. Traditionally, MEMS are made from heavily-doped silicon, which at best has a resistivity about the same as the MoO_xC_y-CNT composite we have made (see Table 3.1). Therefore, CNT-M could create MEMS with resistivities at least as good as those obtained by methods such as DRIE, and it could do so without the effort that goes into obtaining heavily doped silicon.

3.4 Strength

Due to the difficulty of releasing and handling very thin and brittle cantilever beams, we accidentally broke many of the samples prior to strength testing. However, after some trial and error, several experiments succeeded well enough to calculate a ballpark range for the mechanical properties of the MoO_xC_y-CNT composite (see Figure 3.8). From the data we determined that the material has a Young’s modulus between 9.17 and 56.2 GPa, a yield strength between 106 and 221 MPa, and a maximum percent strain between 0.4 and 1.5%. These values characterize

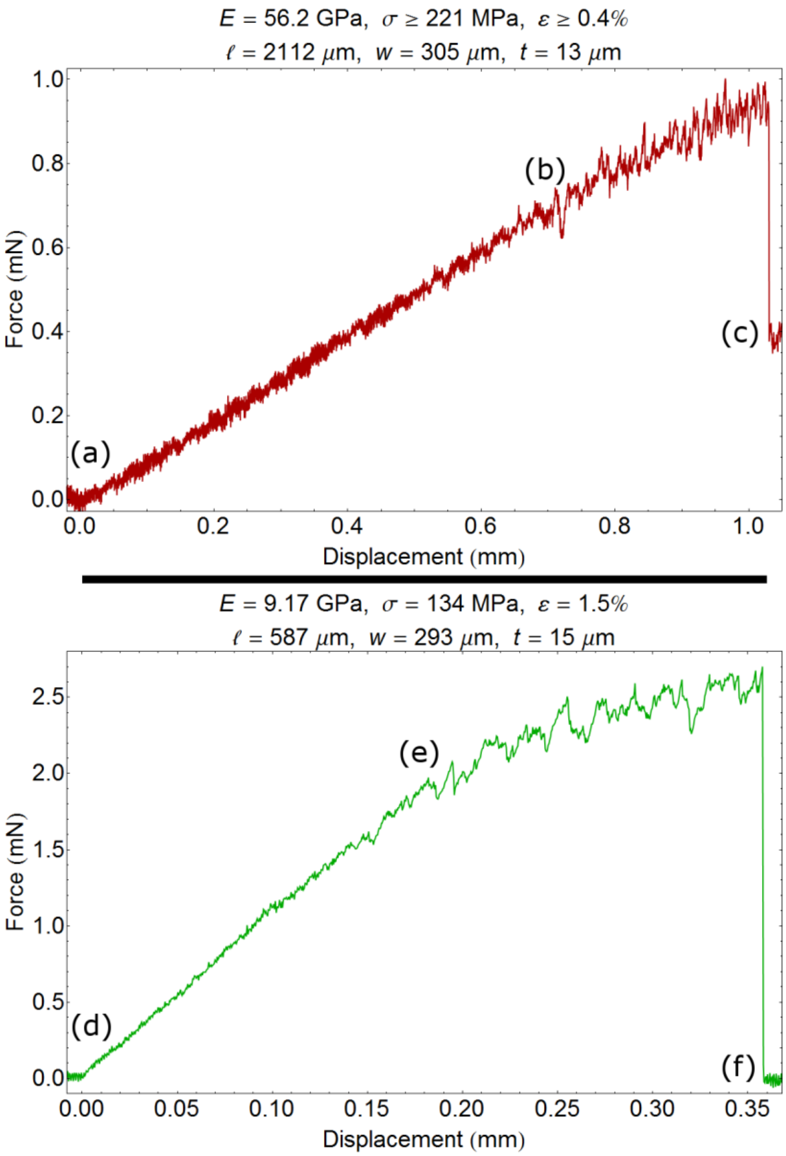

Figure 3.8 Force versus displacement curves. In the two graphs, locations **(a)** and **(d)** mark the beginning of the run, where the Instron brought the force-testing needle into contact with the cantilever beam. **(b)** and **(e)** indicate the location where, due to the deflection of the cantilever, the needle began to slip, as noted by the noise in the subsequent data. The sharp drop at **(c)** and **(f)** typically denotes where the cantilever beam finally broke and the force on the needle returned to zero. However, in the case of **(c)**, the drop was actually due to the needle slipping off the end of the cantilever, as shown in the data.

Material	Resistivity (ρ) in μΩ·cm	Young's Modulus (E) in GPa	Yield Strength (σ) in MPa
Aluminum	2.4 – 7.5	70 – 79	20 – 50
Nickel	6.1 – 10	170 – 210	140 – 195
CNT	30 – 1000	200 – 950	11000 – 63000
MoO_xC_y-CNT	749 – 935	9.17 – 56.2	106 – 221
Silicon	$5\times10^2 – 3\times10^{11}$	129 – 186	4700 – 7000
Wood	$10^{11} – 10^{24}$	10 – 14	30 – 210

Table 3.1 Comparison with common materials' average electrical and mechanical properties. Different fabrication conditions are what lead to the range in values. The data here show that the CNT composite is both conductive and strong.

the material as brittle, but strong (see Table 3.1).

One potential method for increasing the flexibility of the MoO_xC_y-CNT composite would be to anneal the sample at high temperatures, because a high-temperature anneal would cause the atomic structure of the deposited film to purify and change. Out of curiosity, we performed a thermal anneal on one of our samples at 900°C for 10 minutes in H_2, and we found that most of the structures decreased in size, possibly due to a volume reduction as impurities were removed (see Figure 3.9). Testing the electrical and mechanical properties of annealed structures still needs to be done.

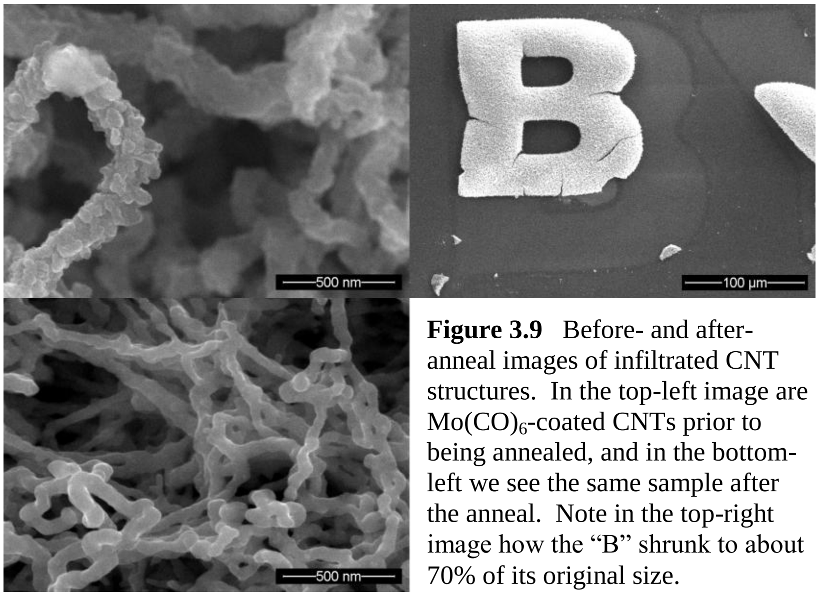

Figure 3.9 Before- and after-anneal images of infiltrated CNT structures. In the top-left image are $Mo(CO)_6$-coated CNTs prior to being annealed, and in the bottom-left we see the same sample after the anneal. Note in the top-right image how the "B" shrunk to about 70% of its original size.

We believe that the large spread in calculated values for the mechanical properties of the composite is in large part due to the variability of the extent of infiltration (see Figure 3.10). The sample with the highest strength also had the shortest growth and best infiltration, whereas those samples that were slightly taller didn't infiltrate as completely

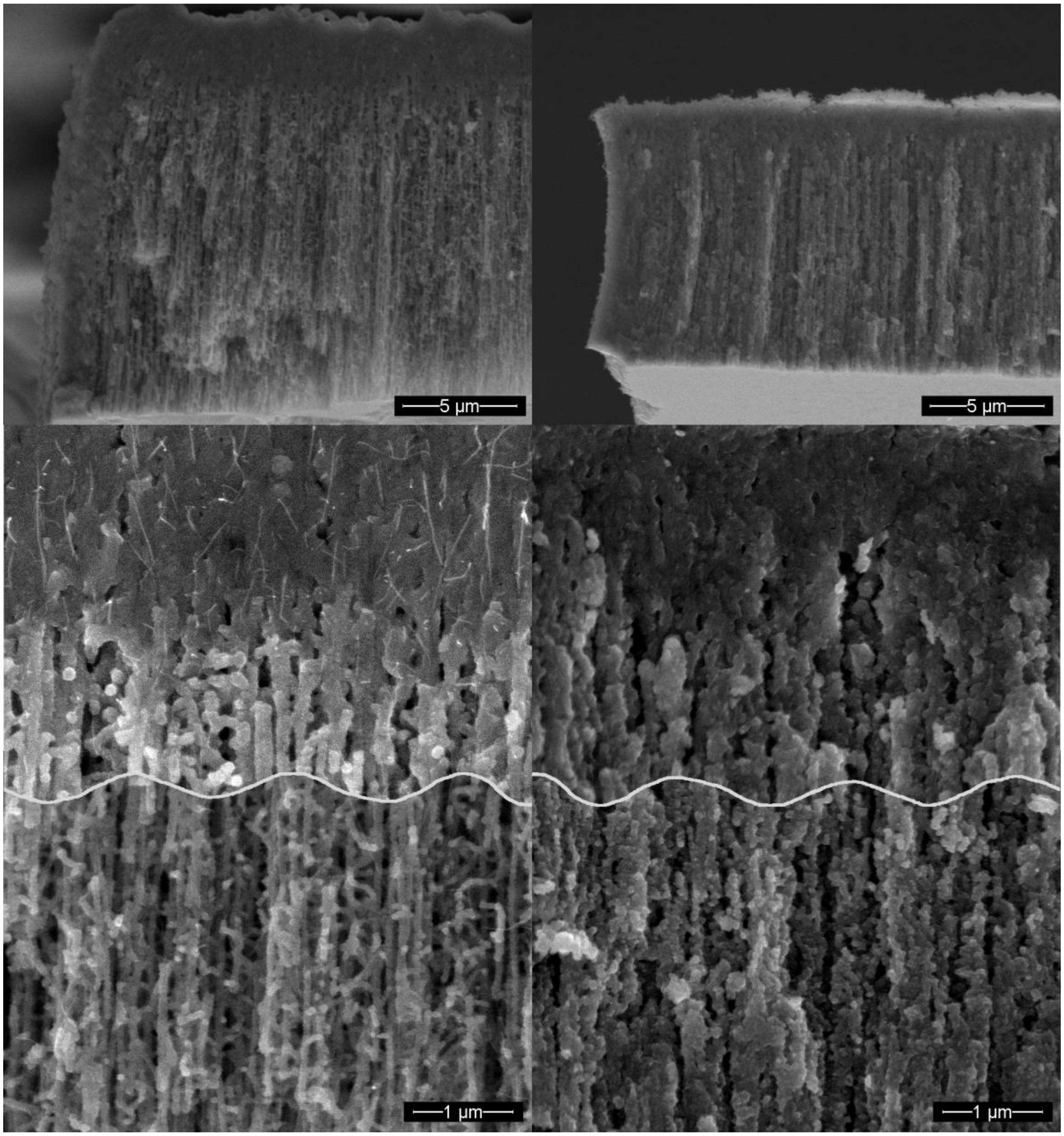

Figure 3.10 Variability in the extent of infiltration due to sample height variations. The two samples above were infiltrated using the same parameters, but during mechanical testing the sample on the right showed it had a much higher Young's modulus and yield strength. It turned out that the forest height was 2 μm shorter than the sample on the left, and thus we see the infiltration reaching the bottom of the forest was more complete, resulting in a stronger, albeit more brittle, structure.

and had lower strength values. In addition to the differences in sample height and thus infiltration, defects in the CNT structures caused during growth or infiltration may have contributed to the large range of values.

3.5 Conclusions and Future Outlook

Through this study we have developed a new composite material for fabricating high-aspect-ratio microstructures with both relatively high mechanical strength and good electrical conductivity. We sought to optimize the CNT-M method for creating metallic microstructures, found that using $Mo(CO)_6$ as a CVD precursor rather than $W(CO)_6$ made fuller infiltrations more possible, and we tested the mechanical and electrical properties of the resulting MoO_xC_y-CNT composite material. Through the van der Pauw method, the material was shown to have an electrical resistivity between 749 and 935 $\mu\Omega\cdot$cm, and by deflecting cantilever beams we found the material had a Young's modulus between 9.17 and 56.2 GPa, a yield strength between 106 and 221 MPa, and a maximum percent strain between 0.4 and 1.5%.

Further refinement of the CVD process for infiltrating the CNT forest needs to take place, such as in determining the optimal deposition pressure and gas flow. In addition, there are a number of potential applications for partially-infiltrated CNT structures that should be investigated. For instance, partial infiltration of a CNT forest with a metal could physically stabilize it enough to withstand a second infiltration step via electrodeposition or electroless deposition. Notwithstanding our current lack of complete infiltration, however, the MoO_xC_y-CNT composite has rather desirable properties.

This material not only has potential for future microfabrication applications, but it represents one of the many new materials that CNT-M is capable of producing. With a strong, electrically conductive, refractory material, such as what we have produced, available to the realm of MEMS through a simple fabrication procedure, new MEMS designs could become possible. We hope that with further research the CNT-M method will proliferate throughout the scientific and technological communities, because it has many possibilities that can still be explored.

References

[1] Iijima, Sumio. “Helical microtubules of graphitic carbon.” *Nature* **354** 7 (1991) 56-58.

[2] Dresselhaus, M. S., *et al*. “Electronic, thermal and mechanical properties of carbon nanotubes.” *Phil. Trans. R. Soc. Lond. A* **362** (2004) 2065-2098.

[3] Popov, Valentin N. “Carbon nanotubes: properties and application.” *Mat. Sci. Eng. R* **43** (2004) 61–102.

[4] Huang JiaQi, *et al*. “A review of the large-scale production of carbon nanotubes: The practice of nanoscale process engineering.” *Chin. Sci. Bull.* **57** 2-3 (2012) 157-166.

[5] Terrones, Mauricio. “Science and Technology of the Twenty-First Century: Synthesis, Properties, and Applications of Carbon Nanotubes.” *Annu. Rev. Mater. Res.* **33** (2003) 419-501.

[6] Endo, Morinobu, et al. “Applications of carbon nanotubes in the twenty-first century.” *Phil. Trans. R. Soc. Lond. A* **362** (2004) 2223-2238.

[7] Chen, Hao, et al. “Controlled growth and modification of vertically-aligned carbon nanotubes for multifunctional applications.” *Mater. Sci. Eng. R* **70** (2010) 63-91.

[8] Schnorr, Jan M. and Timothy M. Swager. “Emerging Applications of Carbon Nanotubes.” *Chem. Mater.* **23** (2011) 646-657.

[9] Wang XiaoJing and Liu Zhuang. “Carbon nanotubes in biology and medicine: An overview.” *Chin. Sci. Bull.* **57** 2-3 (2012) 167-180.

[10] Feynman, Richard P. “There’s plenty of room at the bottom.” *Eng. Sci.* **23** (1960) 22-36.

[11] Moore, Gordon E. “Progress in Digital Integrated Electronics.” *Electronics* **38** (1965) 114.

[12] Barth, Johannes V., Giovanni Costantini, and Klaus Kern. “Engineering atomic and molecular nanostructures at surfaces.” *Nature* **437** (2005) 671-679.

[13] Kal, Santiram. “Microelectromechanical Systems and Microsensors.” *Def. Sci J.* **57** 3 (2007) 209-224.

[14] Hooda, Manish K., *et al*. “A systematic study of DRIE process for high aspect ratio microstructuring.” *Vacuum* **84** (2010) 1142–1148.

[15] Malek, Chantal K. and Volker Saile. “Applications of LIGA technology to precision manufacturing of high-aspect-ratio micro-components and -systems: a review.” *Microelectronics J*. **35** (2004) 131–143.

[16] Hayamizu, Y., *et al*. “Integrated three-dimensional microelectromechanical devices from processable carbon nanotube wafers." *Nature Nanotech*. **3** (2008) 289-294.

[17] Meiyong Liao and Yasuo Koide. “Carbon-Based Materials: Growth, Properties, MEMS/NEMS Technologies, and MEM/NEM Switches.” *Crit. Rev. Solid State Mater. Sci.* **36** (2011) 66–101.

[18] Hutchison, David N., *et al*. “High Aspect Ratio Microelectromechanical Systems: A Versatile Approach Using Carbon Nanotubes as a Framework.” *Proc. 15th Int. Conf. on Solid-State Sensors, Actuators and Microsystems*, Denver, CO, Jun 21-25 (2009).

[19] Hutchison, David N. “Vertically Aligned Carbon Nanotubes as a Framework for Microfabrication of High Aspect Ratio MEMS.” Undergraduate thesis, published by Brigham Young University Department of Physics and Astronomy (2008).

[20] Wood, Taylor S. “Mechanical Properties of a-Carbon Infiltrated Carbon Nanotube Templated Materials.” Honors thesis, published by Brigham Young University Honors Department (2011).

[21] Hutchison, David N., *et al*. “Carbon nanotubes as a framework for high aspect ratio MEMS fabrication.” *J. MEMS* **19** 1 (2010) 75-82.

[22] Fazio, Walter C., *et al*. “Materials Properties of Carbon-Infiltrated Carbon Nanotube-Templated Structures for Microfabrication of Compliant Mechanisms.” *Proc. ASME Int. Mechanical Engineering Congress and Exposition*, Denver, CO, Nov 11-17 (2011).

[23] McKenna, David M. “Tungsten Infiltrated Carbon Nanotube Forests As A Framework For 3-D Microfabrication.” Undergraduate thesis, published by Brigham Young University Department of Physics and Astronomy (2011).

[24] McKenna, David M., *et al*. “Carbon Nanotube Templated Microfabrication of High Aspect Ratio Metal Structures.” *Proc. Technologies for Future Micro-Nano Manufacturing*, Napa, CA, Aug 8-10 (2011).

[25] Lander, J. J. and L. H. Germer. “Plating Molybdenum, Tungsten and Chromium by Thermal Decomposition of Their Carbonyls.” *Am. Inst. Min. Metal. Eng. Tech.* Pub. No. 2295, (1947).

[26] Gesheva, K. A., V. Abrosimova, and G. D. Beshkov. “CVD Carbonyl Thin Films of Tungsten and Molybdenum and their Silicides – A Good Alternitive to CVD Fluoride Tungsten Technology.” *J. de Phys. IV Suppl. J. Phys. II*, *1* (1991).

[27] Wei, Wen-Cheng J. and Ming-Hung Lo. “Processing and Properties of (Mo,Cr) Oxycarbides from MOCVD.” *Appl. Organometal. Chem.* **12** (1998) 201-220.

[28] Cho, C. C. and S. L. Bernasek. “Molybdenum deposition from the decomposition of molybdenum hexacarbonyl.” *J. Appl. Phys.* **65**, 8 (1989) 3035-3043.

[29] Isobe, Y., *et al*. “Structure and thermal resistance of chemically vapor deposited molybdenum on graphite.” *J. Vac. Sci. Technol.* A **4**, 6 (1986) 3046-3049.

[30] Carver, G. E. and B. O. Seraphin. “Chemical-vapor-deposited molybdenum films of high infrared reflectance.” *Appl. Phys. Lett.* **34**, 4 (1979) 279-281.

[31] van der Pauw, L. J. “A Method of Measuring Specific Resistivity and Hall Effect of Discs of Arbitrary Shape.” *Phillips Res. Repts.* **13** (1958) 1-9.

[32] Weihs, T.P., *et al*. “Mechanical deflection of cantilever microbeams: A new technique for testing the mechanical properties of thin film.” *J. Mater. Res.* **3**, 5 (1988) 931-42.